PERGAMON

International Journal of Heat and Mass Transfer 43 (2000) 4087–4100

International Journal of HEAT and MASS TRANSFER

www.elsevier.com/locate/ijhmt

Buoyancy-driven flow and heat transfer in open-ended enclosures: elimination of the extended boundaries

K. Khanafer, K. Vafai

Department of Mechanical Engineering, Ohio State University, 206 West 18th Avenue, Columbus, OH 43210-1107, USA

Received 28 September 1999; received in revised form 28 January 2000

Abstract

The present study is focused on obtaining an accurate representation of effective boundary conditions at the open side of two- and three-dimensional open-ended structures. Implementation of this representation reduces the more complicated open-ended boundary conditions to a closed-ended domain and results in substantial savings in CPU and memory usage. The numerical procedure used in this work is based on the Galerkin weighted residual method of finite-element formulation. Comparisons between the present investigation using the correlations for the proposed closed-ended model and the results for the extended computational domain attest to the successful implementation of the proposed model. The results presented in this work constitute an innovative way to describe correctly the boundary conditions at the open side of an open-ended boundary.

Keywords: Natural convection; Two- and three-dimensional; Open-ended structure; Effective boundary conditions

1. Introduction

Natural convection in open-ended enclosures has received increasing attention in recent years because various practical applications can be modeled around the basic geometry associated with such a configuration. Such applications include solar thermal receiver systems, fire research, cooling of electronic equipment and energy conservation in buildings. One of the main characteristics of buoyancy-driven flows and heat transfer in open-ended cavities is its basic geometry, which reveals the interactions and the influence of the inner and outer regions of the cavity on the flow and temperature fields. Penot [1] conducted a numerical study of two-dimensional (2D) natural convection in an isothermal open square enclosure.

The same configuration with variable properties using primitive variables was studied by LeQuere et al. [2]. The results of this study showed that the flow unsteadiness arises for large values of Grashof number and that the flow field approaching the open cavity depends on the far field boundary conditions.

Other Problems involving natural convection in open enclosures were studied by Doria [3] for predicting unsteady flows of multicomponent gases with strong Buoyancy effects and by Jacobs et al. [4,5] in modeling circulation above city streets and geothermal reservoirs. Experimental studies were also conducted by Humphrey and co-workers [6] and Sernas and Kyriakides [7] in modeling solar systems. Chan and Tien [8] performed a numerical steady-state study of laminar natural convection in a 2D square open cavity with a heated vertical wall and two insulated horizontal walls. The results of this study illustrated the effect of the open boundary on the basic flow patterns. Later on, the same authors [9] investigated numerically laminar steady-state natural convection in a 2D rectangular open

0017-9310/00/$ - see front matter
PII: S0017-9310(00)00047-8

Nomenclature

A	aspect ratio of the enclosure (for 2D: $A = w/H$ and for 3D: $A = \frac{R_2}{R_1}$)
c_p	specific heat at constant pressure, J kg^{-1} K^{-1}
g	acceleration due to gravity, m s^{-2}
H	height of the enclosure, m
k	thermal conductivity, W m^{-2} K^{-1}
L	length of the annular enclosure, m
L_e	length of the extended computational domain for the 3D configuration, m
L_x	extended computational domain length in x-direction for the 2D configuration, m
L_y	extended computational domain length in y-direction for the 2D configuration, m
n	outward normal to a surface
Nu	Nusselt number
p	pressure, Pa
P	dimensionless pressure
Pr	Prandtl number ($\frac{\nu}{\alpha}$)
q	heat flux vector
R_1	radius of the inner cylinder, m
R_2	radius of the outer cylinder, m
Ra	Rayleigh number ($\frac{g\beta L^3 \Delta T}{\nu\alpha}$)
t	time, s
T_1	temperature of the inner cylinder, °C
T_2	temperature of the outer cylinder, °C
T_w	enclosure wall temperature, °C
T^*	dimensionless temperature (3D model)
Θ	dimensionless temperature (2D model)
U	dimensionless velocity in the x-direction
V	dimensionless velocity in the y-direction
W	dimensionless velocity in the z-direction
w	width of the enclosure, m
u_r	velocity in the r direction, m s^{-1}
u_θ	velocity in the θ direction, m s^{-1}
x, y, z	Cartesian coordinates, m
r, θ	cylindrical coordinates

Greek symbols

α	thermal diffusivity, m^2 s^{-1}
β	coefficient of volume expansion, K^{-1}
μ	dynamic viscosity, kg m^{-1} s^{-1}
ν	kinematic viscosity, m^2 s^{-1}
ρ	density, kg m^{-3}
τ	dimensionless time

Subscripts

1	inner cylinder
2	outer cylinder
∞	condition at infinity

cavity by imposing approximate boundary conditions at the open side of the enclosure.

A comprehensive study was conducted by Vafai and Ettefagh [10,11] for investigating basic aspects and physics of the flow field within the open-ended structures and the effect of extended computational domain on flow and heat transfer inside the open-ended cavity and its immediate surroundings. Vafai and Ettefagh [10,11] established that the extent of the enlarged computational domain has a substantially larger effect than previously reported by other investigators.

Most of the three-dimensional (3D) numerical investigations were performed for rectangular enclosures [12–17]. Only a few numerical studies in the past decade were based on a concentric annulus. Ozoe et al. [18] solved numerically the buoyancy-induced flow problem in a vertical annulus heated from below using the modified vorticity-vector approach. Later on, Ozoe et al. [19] investigated experimentally and numerically the effects of inclination angle for the same problem. Takata et al. [20] performed a study of 3D laminar natural convection in an inclined cylindrical annulus with heated inner and cooled outer cylinders for a very high Prandtl number. Vafai and Ettefagh [21] performed an investigation of transient 3D buoyancy-driven flow and heat transfer in a horizontal annulus bounded by two impermeable boundaries in the axial direction. The results showed that the temperature distribution remains unchanged in the core region provided that the annulus length to the outer radius ratio was larger than a critical value. Vafai and Ettefagh [22] also investigated the 3D natural convection inside an open-ended annulus in which the inner cylinder was maintained at a higher temperature. The results of this study revealed the existence of a core region for $Ra < 10^4$ in which the thermal characteristics were weakly dependent on the axial conduction. Moreover, it was observed that a 2D approximation for the problem within the core region produced accurate results for early times during the development of the flow field. Comparative analysis of the finite-element and finite-difference methods for simulation of buoyancy-induced flow and heat transfer in closed and open-ended annular cavities was also performed by Vafai and Desai [23].

The main difficulty associated with the study of fluid flow in open-ended structure is the specification of the boundary conditions at the open end. Most numerical

studies of open cavities rely on solving the governing equations in a domain extended outside the opening side of the enclosure and applying the far field conditions at the boundary of the extended domain. Vafai and Ettefagh [21,22] have shown that the extent of the extended computational domain must be much larger than previously utilized and as such they have shown substantial inaccuracies associated with the later approach.

The extension of the open-ended domain requires substantially larger memory and computational time. An appropriate set of boundary conditions at the aperture plane of the open-ended structure will drastically reduce the memory and time requirements. The present work focuses on modeling an accurate representation of the boundary conditions at the open side of the enclosure. In this approach, the velocity and temperature variations at the aperture plane are correlated in terms of the controlling parameters. In this investigation, two- and three-dimensional open-ended structures are analyzed. The computations will be performed using both an extended outer computational domain as well as elimination of the extended domain through appropriate modeling thus reducing the problem to a closed-ended structure.

2. Comparitive analysis for the two-dimensional open-ended enclosure

2.1. Physical model and assumptions

The fundamental physical model and coordinate system for the open-ended enclosure under consideration are illustrated in Fig. 1. This model is similar to the configuration used by Chan and Tien [8]. The problem is modeled as a 2D, incompressible, unsteady natural convection. The fluid physical properties are assumed constant and the Boussinesq approximation is invoked.

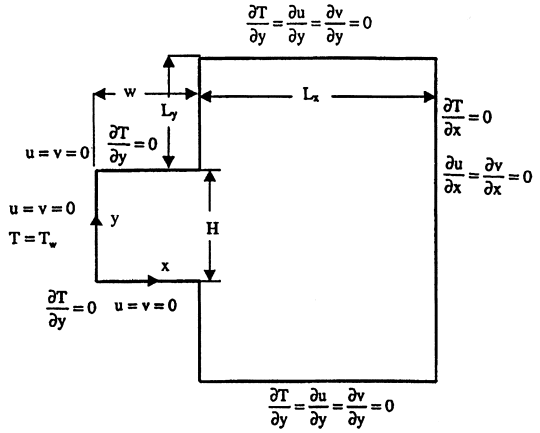

Fig. 1. Physical domain and coordinate system.

The governing equations for the problem under consideration are based on the balance laws for mass, linear momentum, and thermal energy. Taking into account the above mentioned assumptions, these equations, expressed in non-dimensional form, can be written as

$$\frac{\partial U}{\partial X}+\frac{\partial V}{\partial Y}=0 \tag{1}$$

$$\sqrt{\frac{Ra}{Pr}}\left(\frac{\partial U}{\partial \tau}+U\frac{\partial U}{\partial X}+V\frac{\partial U}{\partial Y}\right)=\frac{\partial P}{\partial X}+\left(\frac{\partial^2 U}{\partial X^2}+\frac{\partial^2 U}{\partial Y^2}\right) \tag{2}$$

$$\sqrt{\frac{Ra}{Pr}}\left(\frac{\partial V}{\partial \tau}+U\frac{\partial V}{\partial X}+V\frac{\partial V}{\partial Y}\right)=\frac{\partial P}{\partial Y}+\left(\frac{\partial^2 V}{\partial X^2}+\frac{\partial^2 V}{\partial Y^2}\right)+\sqrt{\frac{Ra}{Pr}}\Theta \tag{3}$$

$$\sqrt{\frac{Ra}{Pr}}\left(\frac{\partial \Theta}{\partial \tau}+U\frac{\partial \Theta}{\partial X}+V\frac{\partial \Theta}{\partial Y}\right)=\frac{\partial^2 \Theta}{\partial X^2}+\frac{\partial^2 \Theta}{\partial Y^2} \tag{4}$$

where $Ra=\frac{g\beta H^3\Delta T}{\nu\alpha}$ and $Pr=\nu/\alpha$

Eqs. (1)–(4) were cast in nondimensional form by using the following nondimesional variables:

$$\left.\begin{aligned} X&=\frac{x}{H} & Y&=\frac{y}{H} & \tau&=\frac{t\alpha\sqrt{RaPr}}{H^2}\\ U&=\frac{uH}{\alpha\sqrt{RaPr}} & V&=\frac{vH}{\alpha\sqrt{RaPr}} & P&=\frac{pH^2}{\mu\alpha\sqrt{RaPr}}\\ \Theta&=\frac{T-T_\infty}{\Delta T} & \Delta T&=T_w-T_\infty \end{aligned}\right\} \tag{5}$$

In the above equations, u and v are the velocity components in the x- and y-directions, t the time, T the fluid temperature, p the fluid pressure, β the volumetric expansion coefficient, H the height of the enclosure, T_w the enclosure wall temperature, and ν, μ, ρ_o, and c_p are the kinematic viscosity, dynamic viscosity, fluid density, and the specific heat, respectively.

2.2. Initial conditions

The walls of the enclosure are assumed to be initially at a uniform ambient temperature and the fluid is assumed to be stagnant and at ambient temperature

throughout the computational domain. That is

$$U = V = \Theta = 0 \quad \text{at } t = 0 \tag{6}$$

2.3. Boundary conditions

The boundary conditions on the extended computational domain can be written as

1. For the left wall of the enclosure

at $x = 0$

$$u = v = 0 \quad \text{and} \quad T = T_w \tag{7}$$

2. For the upper and lower walls of the enclosure

at $y = 0, H$

$$u = v = \frac{\partial T}{\partial y} = 0 \tag{8}$$

3. For the x-far field open boundaries

at $x = L_x + w$ and $-L_y \leq y \leq L_y + H$

$$\frac{\partial T}{\partial x} = \frac{\partial v}{\partial x} = \frac{\partial u}{\partial x} = 0 \tag{9}$$

4. For the y-far field open boundaries

at $y = -L_y, L_y + H$ and $w \leq x \leq L_x + w$

$$\frac{\partial T}{\partial y} = \frac{\partial v}{\partial y} = \frac{\partial u}{\partial y} = 0 \tag{10}$$

2.4. Numerical scheme

A Galerkin-based FEM is employed to solve the governing equations for the present study. The application of this technique is well described by Taylor and Hood [24] and Gresho et al. [25], and its application is well documented [26]. The segregated solution algorithm is utilized to solve the system of equations. The advantage of using this method is that the global system matrix is decomposed into smaller submatrices and then solved in a sequential manner. This technique will result in considerably fewer storage requirements. The conjugate residual scheme is used to solve the symmetric pressure type equation systems, while the conjugate gradient squared is used for the non-symmetric advection–diffusion type equations. Extensive numerical experimentation was performed to attain grid-independent results for all the field variables.

3. Heat transfer calculations

The Nusselt number is defined as

$$Nu = q_n = \frac{\partial \Theta}{\partial n} \tag{11}$$

where n denotes the outward pointing normal from the surface over which the heat flux is calculated. This definition of the Nusselt number is used to represent all the heat transfer results in the present study.

4. Model validation

Benchmarking of the presented model is considered to be a substantial part of this work. As such, while utilizing the full extent of the extended boundaries, the present model has been compared with the results of Vafai and Ettefagh [10] for different values of Rayleigh number. Figs. 2 and 3 show a very good agreement between the present work utilizing an extended domain and the results reported by Vafai and Ettefagh [10] for open-ended cavity with extended outer boundaries. As an additional check on the accuracy of the present results, Table 1 shows a comparison of the Nusselt number measured at the top and bottom walls of the enclosure.

5. Two-dimensional model based on effective boundary conditions

A comprehensive numerical study was conducted to come up with appropriate boundary conditions for the velocity and temperature fields at the open side of the cavity for various controlling parameters. This was achieved by solving the governing equations for the velocity and temperature fields taking into account the effect of the outer extended boundaries. The results were then correlated in terms of the pertinent controlling parameters. These controlling parameters include the Rayleigh number and the aspect ratio of the enclosure. A wide range of the Rayleigh number was selected for this investigation as $10^3 \leq Ra \leq 10^5$. A wide range of the aspect ratio, $A = w/H$ of the enclosure, was also selected as $0.25 \leq A \leq 1$. For the 2D open cavity case, after extensive set of simulations, the boundary conditions at the open side of the enclosure were found to be well presented by

$$U = a_1 + a_2 Y^{a_3}(Ra^{a_3} A^{a_5}) \tag{12a}$$

where $a_1 = -0.1328$, $a_2 = 0.4073$, $a_3 = 2.4973$, $a_4 = 0.0139$ and $a_5 = 0.0293$.

$$V = b_1 + b_2 Y^{b_3}\left(Ra^{b_4} A^{b_5}\right) \tag{12b}$$

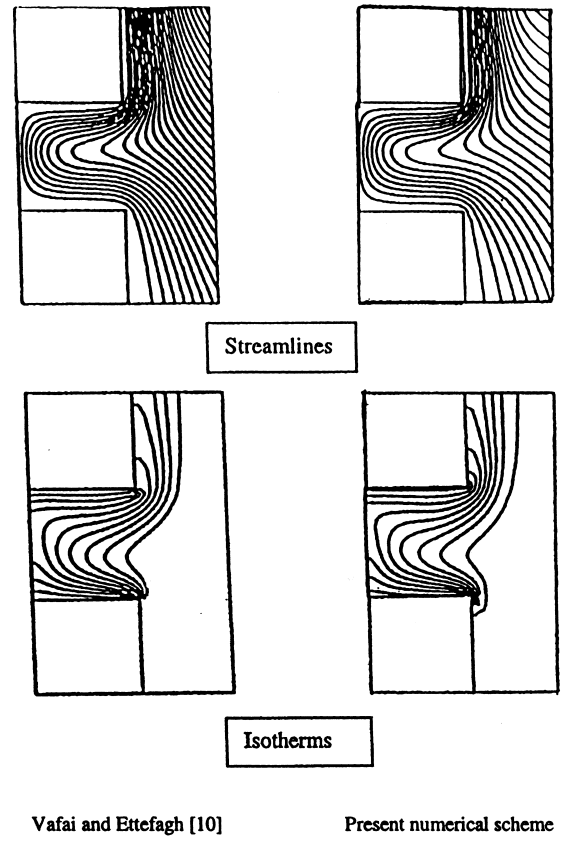

Fig. 2. Comparison of the streamlines and isotherms between the 2D model utilizing the extended boundaries and that of Vafai and Ettefagh [10] for Rayleigh number $Ra = 10^4$.

where $b_1 = 2.541 \times 10^{-3}$, $b_2 = 0.1591$, $b_3 = 0.4940$, $b_4 = -0.0761$ and $b_5 = -0.7238$.

$$\Theta = c_1 Y^4 (Ra^{c_2} A^{c_3}) + c_4 Y^3 \tag{12c}$$

where $c_1 = -0.0164$, $c_2 = 0.2814$, $c_3 = 0.4681$ and $c_4 = 0.8131$.

The validity of the closed-ended model as presented by the above boundary conditions was checked against the results obtained by incorporating the fully extended outer boundary conditions for the open-ended cavity shown in Fig. 1. Table 2 shows a comparison of the average Nusselt number between the results with and without (the closed-ended model based on the effective boundary conditions) the extended outer boundaries. The results based on using the closed-ended model show a very good agreement with those using the fully extended outer boundaries.

Table 1
Comparison of the average Nusselt numbers between the present numerical scheme and the 2D results of Vafai and Ettefagh [10] for various Rayleigh numbers

	Present	Vafai and Ettefagh [10]	Percent difference (%)
$Ra = 10^4$			
Nu (lower)	1.99	2.0	0.5
Nu (upper)	1.09	1.05	3.8
$Ra = 10^5$			
Nu (lower)	3.15	2.98	5.7
Nu (upper)	2.9	3.1	6.5

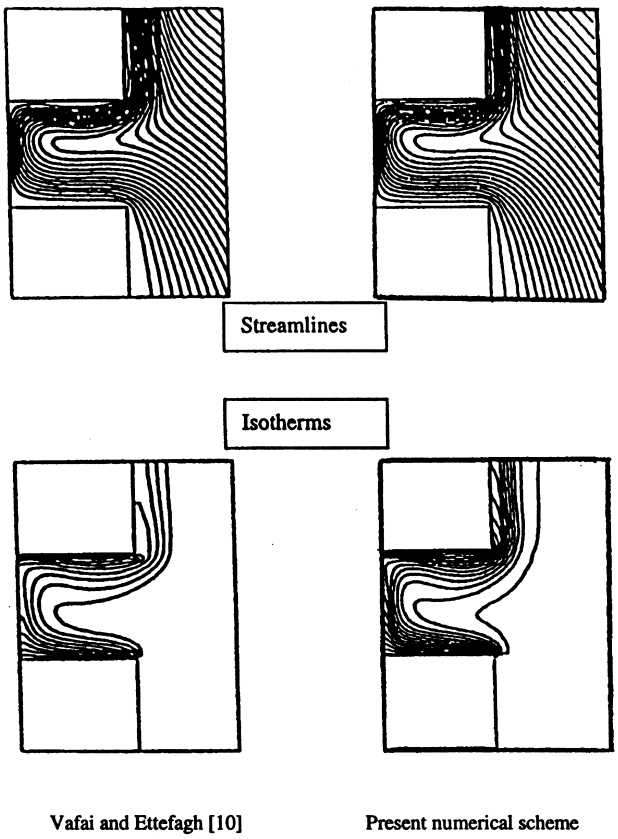

Fig. 3. Comparison of the streamlines and isotherms between the 2D model utilizing the extended boundaries and that of Vafai and Ettefagh [10] for Rayleigh number $Ra = 10^5$.

6. Comparative analysis for the three-dimensional open-ended annular enclosures

6.1. Physical model and assumptions

The fundamental physical model and the coordinate system used in this part of the investigation are shown in Fig. 4. An inner cylinder of radius R_1 and the outer cylinder of radius R_2 bound the fluid. Due to axial symmetry, one half of the total axial domain is considered. As such, one end of the annulus behaves as a mid-axial symmetry plane while the other end is open to the ambient surrounding. The annulus is situated horizontally. The heated inner cylinder surface and the cooled outer cylinder surface are maintained at constant temperatures T_1 and T_2, respectively. Due to symmetry considerations in the angular direction, one half of the annulus needs to be considered as shown in Fig. 4. It is again assumed that the thermophysical properties of the fluid are independent of temperature

Table 2
Comparison of the average Nusselt numbers between the present model (no outer boundaries) and the results based on utilizing the fully extended outer boundaries ($A = 1$)

Ra/Nu	Present (with outer boundaries)	Present (closed-ended model)	Percentage error (%)
1×10^3	1.051	1.178	12.08
0.5×10^4	2.423	2.272	6.23
1×10^4	3.36	3.082	8.27
0.5×10^5	6.0933	5.7991	4.83
1×10^5	7.56	7.35	2.78

except for the density variation in the buoyancy term where the Boussinesq approximation is invoked.

6.2. Model equations

The non-dimensional governing equations for the 3D open-ended annulus investigation can be written as

$$\frac{\partial u_r}{\partial r}+\frac{u_r}{r}+\frac{1\partial u_\theta}{r\partial\theta}+\frac{\partial u_x}{\partial x}=0 \tag{13}$$

$$\sqrt{\frac{Ra}{Pr}}\left(\frac{\partial u_x}{\partial\tau}+u_r\frac{\partial u_x}{\partial x}+\frac{u_\theta\partial u_x}{r\partial\theta}+u_x\frac{\partial u_x}{\partial x}\right)=\frac{\partial P}{\partial x}+\left[\frac{1}{r}\frac{\partial}{\partial r}\left(r\frac{\partial u_x}{\partial r}\right)+\frac{1}{r^2}\frac{\partial^2 u_x}{\partial\theta^2}+\frac{\partial^2 u_x}{\partial x^2}\right] \tag{14}$$

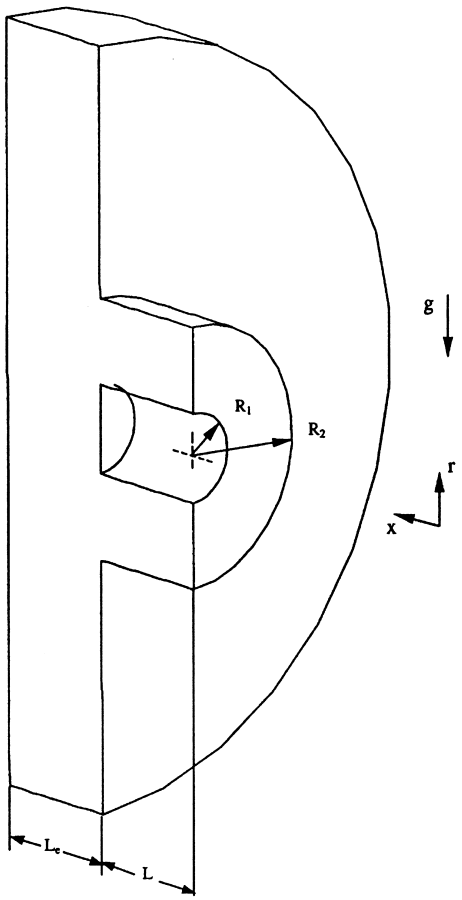

Fig. 4. Physical domain and coordinate system for 3D open-ended annulus.

$$\sqrt{\frac{Ra}{Pr}}\left(\frac{\partial u_r}{\partial\tau}+u_r\frac{\partial u_r}{\partial r}+\frac{u_\theta\partial u_r}{r\partial\theta}-\frac{u_\theta^2}{r}+u_x\frac{\partial u_r}{\partial x}\right)=-\frac{\partial P}{\partial r}+\left[\frac{\partial}{\partial r}\left(\frac{1}{r}\frac{\partial(ru_r)}{\partial r}\right)+\frac{1}{r^2}\frac{\partial^2 u_r}{\partial\theta^2}-\frac{2}{r^2}\frac{\partial^2 u_r}{\partial x^2}+\frac{\partial^2 u_r}{\partial x^2}\right]+\sqrt{\frac{Ra}{Pr}}(T)\cos\theta \tag{15}$$

$$\sqrt{\frac{Ra}{Pr}}\left(\frac{\partial u_\theta}{\partial\tau}+u_r\frac{\partial u_\theta}{\partial r}+\frac{u_\theta\partial u_\theta}{r\partial\theta}+\frac{u_r u_\theta}{r}+u_x\frac{\partial u_\theta}{\partial x}\right)=\frac{-1}{r}\frac{\partial P}{\partial\theta}+\left[\frac{\partial}{\partial r}\left(\frac{1}{r}\frac{\partial(ru_\theta)}{\partial r}\right)+\frac{1}{r^2}\frac{\partial^2 u_\theta}{\partial\theta^2}+\frac{2}{r^2}\frac{\partial u_r}{\partial\theta}+\frac{\partial^2 u_\theta}{\partial x^2}\right]+\sqrt{\frac{Ra}{Pr}}(T)\sin\theta \tag{16}$$

$$\sqrt{\frac{Ra}{Pr}}\left(\frac{\partial T}{\partial\tau}+u_r\frac{\partial T}{\partial r}+\frac{u_\theta\partial T}{r\partial\theta}+\frac{u_r u_\theta}{r}+u_x\frac{\partial T}{\partial x}\right)=\frac{\partial^2 T}{\partial r^2}+\frac{1}{r}\frac{\partial T}{\partial r}+\frac{1}{r^2}\frac{\partial^2 T}{\partial\theta^2}+\frac{\partial^2 T}{\partial x^2} \tag{17}$$

It should be noted that due to the physical nature of the problem a different non-dimensional temperature was used for the 3D case as compared to that for the 2D case. The following dimensionless parameters have been used, and the superscripts in Eqs. (13)–(17) have been dropped for convenience:

$$\left.\begin{aligned} &x^*=\frac{x}{L}; && r^*=\frac{r}{L}; && t=\frac{t\alpha\sqrt{RaPr}}{L^2}\\ &u_x^*=\frac{u_x L}{\alpha\sqrt{RaPr}}; && u_r^*=\frac{u_r L}{\alpha\sqrt{RaPr}}; && u_\theta^*=\frac{u_\theta L}{\alpha\sqrt{RaPr}}\\ &T^*=\frac{T-T_2}{T_1-T_2}; && P^*=\frac{pL^2}{\mu\alpha\sqrt{RaPr}} \end{aligned}\right\} \tag{18}$$

Eqs. (13–17) along with the appropriate initial and boundary conditions fully describe the convective heat transfer process in an open-ended structure.

6.3. Initial conditions

In the present investigation, all the walls of the open-ended annulus are assumed to be initially at a uniform ambient temperature and the fluid is assumed to be stagnant and at ambient temperature throughout the computational domain. Thus, we have

$$u_x=u_r=u_\theta=T=0 \quad \text{at } t=0 \tag{19}$$

6.4. Boundary conditions

The physical domain for the present investigation was extended for implementing the virtually unknown boundary conditions at the open end. The boundary conditions on the extended computational domain can be written as

1. For the axial symmetry planne:

$$\text{at } x = 0 \quad \text{and} \quad \frac{R_1}{L} \le r \le \frac{R_2}{L}$$

$$u_x = 0, \quad \frac{\partial u_r}{\partial x} = \frac{\partial u_\theta}{\partial x} = \frac{\partial T}{\partial x} = 0 \tag{20}$$

2. For the curved surface of the inner cylinder:

$$\text{at } r = \frac{R_1}{L} \quad \text{and} \quad 0 \le x \le 1$$

$$u_x = u_r = u_\theta = 0, \quad T = 1 \tag{21}$$

3. For the vertical surface of the inner cylinder:

$$\text{at } x = 1 \quad \text{and} \quad 0 \le r \le \frac{R_1}{L}$$

$$u_x = u_r = u_\theta = 0, \quad \frac{\partial T}{\partial x} = 0 \tag{22}$$

4. For the curved surface of the outer cylinder:

$$\text{at } r = R_2/L \quad \text{and } 0 \le x \le 1$$

$$u_x = u_r = u_\theta = 0, \quad T = 0 \tag{23}$$

5. For the curved surface of the extension:

$$\text{at } r = \frac{R_e}{L} \quad \text{and} \quad 1 \le x \le \frac{L + L_e}{L}$$

$$\frac{\partial u_x}{\partial r} = \frac{\partial u_r}{\partial r} = \frac{\partial u_\theta}{\partial r} = \frac{\partial T}{\partial r} = 0 \tag{24}$$

6. For the vertical surface of the extension

$$\text{at } x = \frac{L + L_e}{L} \quad \text{and} \quad 0 \le r \le \frac{R_e}{L}$$

$$\frac{\partial u_x}{\partial x} = \frac{\partial u_r}{\partial x} = \frac{\partial u_\theta}{\partial x} = \frac{\partial T}{\partial x} = 0 \tag{25}$$

7. For the vertical surface of the extension at the plane of the opening of the annulus:

$$\text{at } x = 1 \quad \text{and} \quad \frac{R_2}{L} \le r \le \frac{R_e}{L}$$

$$\frac{\partial u_x}{\partial x} = \frac{\partial u_r}{\partial x} = \frac{\partial u_\theta}{\partial x} = \frac{\partial T}{\partial x} = 0 \tag{26}$$

8. For the angular symmetry plane:

$$\text{at } \theta = 0 \quad \text{and} \quad \pi$$

$$u_\theta = 0 \; and \; \frac{\partial u_r}{\partial \theta} = \frac{\partial u_x}{\partial \theta} = \frac{\partial T}{\partial \theta} = 0 \tag{27}$$

7. Three-dimensional model based on effective boundary conditions

A comprehensive numerical study was condcted to arrive at the proper set of boundary conditions for the velocity and temperature fields at the open boundary for the 3D model. However, first the results for the present 3D numerical algorithm are compared with the results of Vafai and Ettefagh [21] for a 3D closed-ended annulus and to Vafai and ettefagh [22] for an open-ended annulus. Fig. 5 shows a very good agreement between the present numerical scheme and the results reported by Vafai and Ettefagh [21] for a closed annular enclosure. The comparison of results with an open-ended enclosure [22] is shown in Fig. 6. An additional evaluation of the accuracy of the present numerical scheme is made by comparing the average Nusselt number at the inner and outer cylinders for both solutions. Table 3 shows an excellent agreement between the two solutions.

For the 3D open-ended annular enclosure, the governing equations are solved for a comprehensive set of controlling parameters in order to obtain a reasonable representation for the temperature and velocity fields at the open side of the enclosure. A wide range of the controlling parameters were selected: Rayleigh number $10^3 \le Ra \le 10^5$, and aspect ratio $1.5 \le A = R_2/R_1 \le 4$. The boundary conditions at the open side of the enclosure were found to be well represented by the following set of correlations

$$U = a_1 YZ(RaA)^{a_2} + a_3 (YZ)^2 (RaA)^{a_4} + a_5 \tag{28a}$$

Table 3
Comparison of the average Nusselt number between the present numerical scheme and that of Vafai and Ettefagh for the 3D results [22]

	Inner cylinder	Outer cylinder
Present	1.70	1.14
Vafai and Ettefagh [25]	1.60	1.10

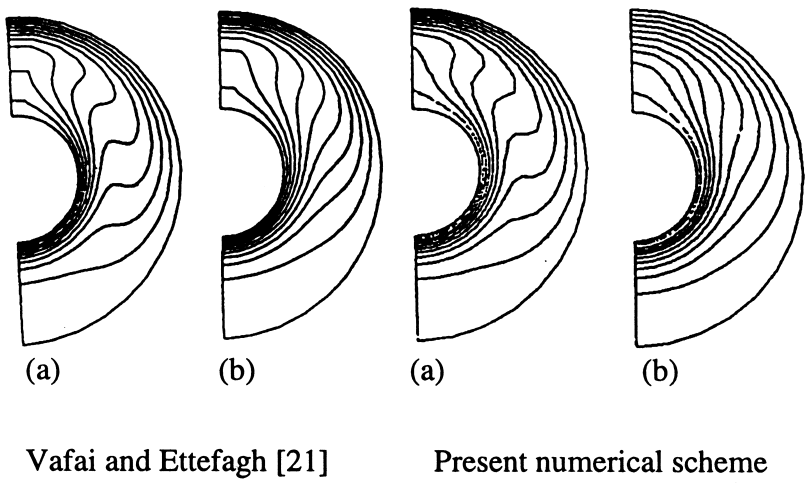

Fig. 5. Comparison of the streamlines and isotherms ($Ra = 4.3 \times 10^4$) between the present numerical scheme and that of Vafai and Ettefagh [21] at different locations: (a) mid-axial plane; and (b) end wall.

where $a_1 = -0.7971$, $a_2 = -0.5282$, $a_3 = -5.744 \times 10^{-3}$, $a_4 = 0.4224$ and $a_5 = 2.464 \times 10^{-3}$.

$$V = b_1 YZ(RaA)^{b_2} + b_3(YZ)^2(RaA)^{b_4} + b_5 \tag{28b}$$

where $b_1 = 0.05949$, $b_2 = 0.06877$, $b_3 = -4.699 \times 10^{-3}$, $b_4 = 0.2221$ and $b_5 = 1.661 \times 10^{-2}$.

$$W = c_1 YZ(RaA)^{c_2} + c_3(YZ)^2(RaA)^{c_4} + c_5 \tag{28c}$$

where $c_1 = 3.305 \times 10^{-3}$, $c_2 = 0.2566$, $c_3 = -1.13 \times 10^{-2}$, $c_4 = 0.2378$, $c_5 = 6.602 \times 10^{-2}$.

$$T = d_1 YZ(RaA)^{d_2} + d_3(YZ)^2(RaA)^{d_4} + d_5 \tag{28d}$$

where $d_1 = -1.606 \times 10^{-2}$, $d_2 = 0.188$, $d_3 = -3.012 \times 10^{-2}$, $d_4 = 0.1878$ and $d_5 = 0.4428$.

The validity of the correlations given in Eq. (28) for the 3D closed-ended model was checked against the results obtained for an enlarged computational domain accounting for the extended outer boundaries. Tables 4–6 show a comparison of the average Nusselt number between the results using the closed-ended 3D model and the results obtained for the fully extended domain. The results for the closed-ended 3D model (based on utilization of the effective boundary conditions) show a very good agreement with those results obtained for the case using extended open-ended domain as seen in Tables 4–6. Detailed comparisons between the 3D closed-ended model and the fully extended domain model are given in Figs. 7–9. Figs. 7–9 show a very good agreement between the two models for the field variables.

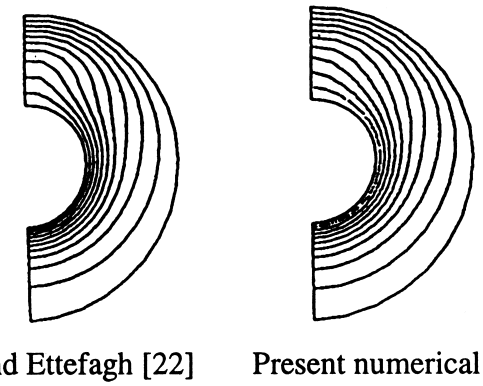

Fig. 6. Comparison of the streamlines and isotherms ($Ra = 10^4$) for open ended-annulus between the present numerical scheme and that of Vafai and Ettefagh [22] at the mid-axial plane.

Table 4
Comparison of the average Nusselt numbers between the present model (no outer boundaries) and results utilizing an extended open-ended domain ($A = 2.6$)

Ra/Nu	Present (with outer boundaries)	Present (no outer boundaries) using effective BCs	Percentage error (%)
Inner cylinder			
1×10^4	3.102	2.944	3.1
4.3×10^4	4.539	4.11	9.45
Outer cylinder			
1×10^4	1.296	1.506	16.20
4.3×10^4	1.872	2.05	9.51

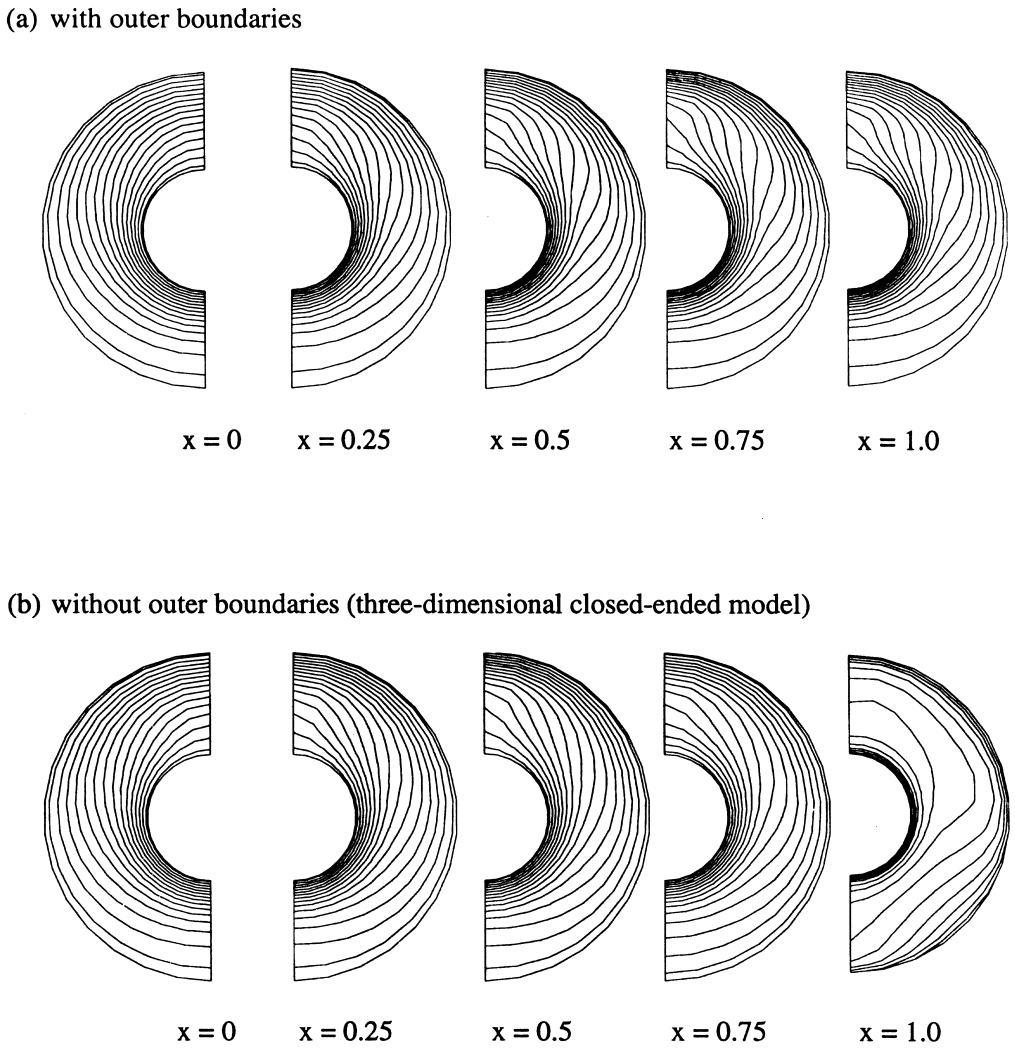

Fig. 7. Comparison of the temperature contours between the 3D closed-ended model based on using extended outer boundaries at different locations for $Ra = 1 \times 10^4$ and $R_2/R_1 = 2.6$.

Table 5
Comparison of the average Nusselt numbers between the present model (no outer boundaries) and results utilizing an extended open-ended domain ($A = 3.0$)

Ra/*Nu*	Present (with outer boundaries)	Present (no outer boundaries) using effective BCs	Percentage error (%)
Inner cylinder			
1×10^4	3.268	2.960	9.42
4.3×10^4	4.585	4.093	10.73
Outer cylinder			
1×10^4	1.20	1.37	14.17
1×10^4	1.611	1.851	14.897

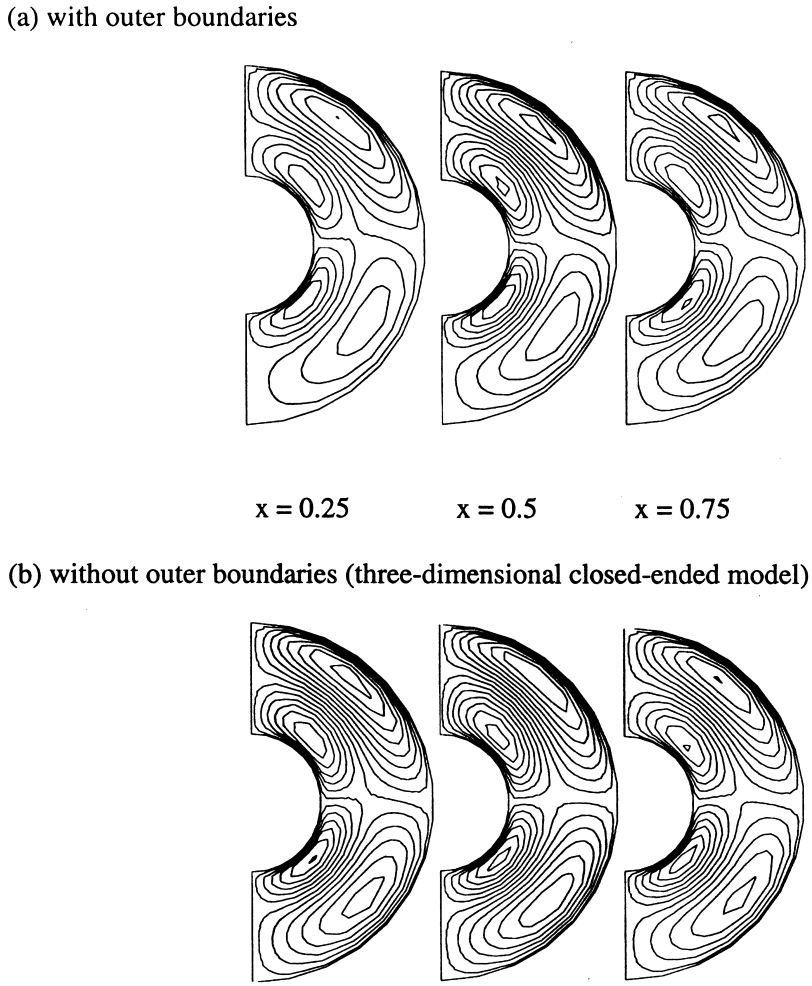

Fig. 8. Comparison of the Y-velocity component contours between the 3D closed-ended model based on using extended outer boundaries at different locations for $Ra = 1 \times 10^4$ and $R_2/R_1 = 2.6$.

Table 6
Comparison of the average Nusselt numbers between the present model (no outer boundaries) and results utilizing an extended open-ended domain ($A = 3.5$)

Ra/Nu	Present (with outer boundaries)	Present (no outer boundaries) using effective BCs	Percentage error (%)
Inner cylinder			
4.3×10^3	2.735	2.526	7.64
1×10^4	3.35	3.04	9.25
4.3×10^4	4.526	4.164	7.99
Outer cylinder			
4.3×10^3	0.876	0.923	5.36
1×10^4	1.064	1.119	5.16
4.3×10^4	1.332	1.536	15.32

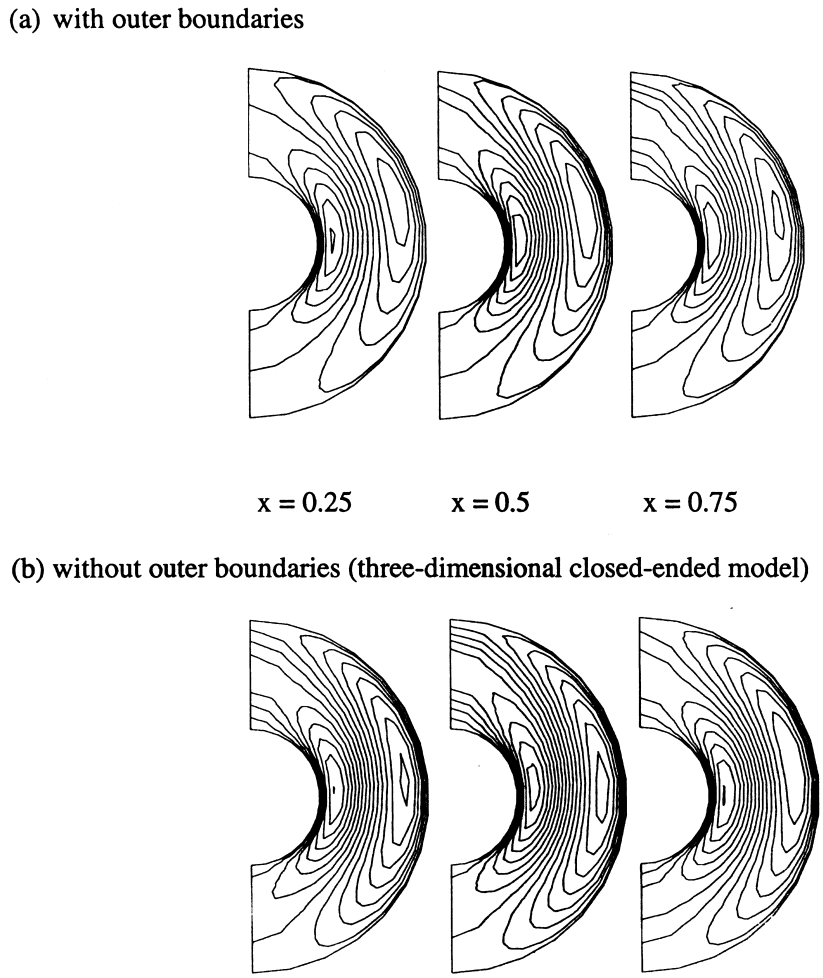

Fig. 9. Comparison of the Z-velocity component contours between the 3D closed-ended model based on using extended outer boundaries at different locations for $Ra = 1 \times 10^4$ and $R_2/R_1 = 2.6$.

Table 7
Comparison of the CPU time reduction for the 2D model at various Rayleigh numbers and an aspect ratio of 1

Ra	CPU (with outer boundaries)	CPU (using effective boundary conditions)	Reduction (%)
1×10^3	109.9	9.96	90.9
0.5×10^4	138.59	12.21	91.2
1×10^4	116.9	14.55	87.6
0.5×10^5	206.09	23.64	88.5

Table 8
Comparison of the CPU time reduction for the 3D model at $Ra = 1 \times 10^4$ and $A = 2.6$

Ra	CPU (with outer boundaries)	CPU (using effective boundary conditions)	Reduction (%)
1×10^4	122.5	36.33	70.3

The main purpose of the cited correlations in Eqs. (12) and (28) is to obtain a large reduction in CPU time and memory usage. The solution for the enlarged computational domain requires large CPU time and memory storage to overcome the problem of unknown boundary conditions for the open-ended region. Tables 7 and 8 show a substantial reduction in CPU time for two- and three-dimensional models using the effective boundary conditions. It can be seen from these tables that there is about 89% reduction in CPU time for 2D model at various Rayleigh numbers and 70% reduction in CPU time at $Ra = 1 \times 10^4$ for 3D model.

8. Conclusions

A comprehensive study for the elimination of the extended boundaries in open-ended structures was presented. Both two and 3D geometries were investigated. An accurate set of effective boundary conditions for both the flow and the temperature fields was obtained covering a comprehensive range of controlling parameters. Detailed comparisons for the Nusselt numbers and the flow and temperature fields were presented between the two and 3D closed-ended models (based on the use of effective boundary conditions) and the fully extended domain simulations indicating very good agreements. The use of the presented two and 3D closed-ended models results in substantial savings in CPU and memory usage and have been shown to compare very well with the fully extended models.

References

[1] F. Penot, Numerical calculation of 2D natural convection in isothermal open cavities, Numer. Heat Transfer 5 (1982) 421–437.
[2] O. LeQuere, J.A.C. Humphery, F.S. Sherman, Numerical calculation of thermally driven 2D unsteady laminar flow in cavities of rectangular croos section, Numer. Heat Transfer 4 (1981) 249–283.
[3] M.L. Doria, A numerical model for the prediction of 2D unsteady flows of multi-component gases with strong buoyancy effects and recirculation, Notre Dame Report, TR-37191-74-4 (1974).
[4] H.R. Jacobs, W.E. Mason, W.T. Hikida, Natural convection in open rectangular cavities, in: Proc. Fifth Int. Heat Transfer Conf., Tokyo, Japan, vol. 3, 1974, pp. 90–94.
[5] H.R. Jacobs, W.E. Mason, Natural convection in open rectangular cavities with adiabatic sidewalls, in: Proc. 1976 Heat Transfer and Fluid Mech. Inst., Stanford University Press, Stanford, 1976, pp. 33–46.
[6] K.S. Chen, J.A.C. Humphery, F.S. Sherman, Experimental investigation of thermally driven flow in open cavities of rectangular cross-section, Phil. Trans. R. Soc. London A316 (1985) 57–84.
[7] V. Serans, I. Kyriakides, Natural convection in an open cavity, in: Proc. Seventh Int. Heat Transfer Conf., Munchen, Germany, vol. 2, 1982, pp. 275–286.
[8] Y.L. Chan, C.L. Tien, A numerical study of 2D natural convection in square open cavities, Numer. Heat Transfer 8 (1982) 65–80.
[9] Y.L. Chan, C.L. Tien, A numerical study of 2D laminar natural convection in shallow open cavities, Int. J. Heat Mass Transfer 28 (1985) 603–612.
[10] K. Vafai, J. Ettefagh, The effects of sharp corners on buoyancy-driven flows with particular emphasis on outer boundaries, Int. J. Heat Mass Transfer 33 (1990) 2311–2328.
[11] K. Vafai, J. Ettefagh, Thermal and fluid flow instabilities in buoyancy-driven flows in open-ended cavities, Int. J. Heat Mass Transfer 33 (1990) 2329–2344.
[12] A. Aziz, J.D. Hellums, Numerical simulations of the

three-imensional equations of motion for laminar natural convection, Phys. Fluids 10 (1976) 314–324.

[13] H. Ozoe, K. Yamamoto, S.W. Churchill, H. Sayama, 3D numerical analysis of laminar natural convection in a confined fluid heated from below, ASME J. Heat Transfer 98C (1976) 202–207.

[14] H. Ozoe, K. Yamamoto, H. Sayama, S.W. Churchill, Natural convection patterns in a long inclined rectangular box heated from below, Int. J. Heat Mass Transfer 20 (1977) 131–139.

[15] H. Ozoe, N. Sato, S.W. Churchill, Experimental confirmation of the 3D helical streaklines previously computed for natural convection in inclined rectangular enclosures, Int. Chem. Eng. 19 (1979) 454–464.

[16] R. Viskanta, D.M. Kim, C. Gau, 3D natural convection heat transfer of a liquid metal in a cavity, Int. J. Heat Mass Transfer 29 (1986) 475–485.

[17] D. Kuhn, P.H. Oosthuzien, 3D transient natural convection flow in a rectangular enclosure with localized heating, Natural Convection in Enclosures 63 (1986) 55–62.

[18] H. Ozoe, T. Okamato, S.W. Churchill, Natural convection in a vertical annular space heated from below, Heat Transfer Jpn. Res. 8 (1979) 82–93.

[19] H. Ozoe, T. Shibata, S.W. Churchill, Natural convection in an inclined circular cylindrical annulus heated and cooled on its end plates, Int. J. Heat Mass Transfer 24 (1981) 727–737.

[20] Y. Takata, K. Iwashige, K. Fukuda, S. Hasegawa, 3D natural convection in an inclined cylindrical annulus, Int. J. Heat Mass Transfer 27 (1984) 747–754.

[21] K. Vafai, J. Ettefagh, An investigation of transient 3D buoyancy-driven flow and heat transfer in a closed horizontal annulus, Int. J. Heat Mass Transfer 34 (1991) 2555–2570.

[22] K. Vafai, J. Ettefagh, Axial transport effects on natural convection inside of an open ended annulus, ASME J. Heat Transfer 113 (1991) 627–634.

[23] K. Vafai, C.P. Desai, Comparative analysis of the finite-element and finite-difference methods for simulation of buoyancy-induced flow and heat transfer in closed and open ended annular cavities, Numer. Heat Transfer 23 (1993) 35–59.

[24] C. Taylor, P. Hood, A numerical solution of the Navier–Stokes equations using finite-element technique, Comput. Fluids 1 (1973) 73–89.

[25] P.M. Gresho, R.L. Lee, R.L. Sani, On the time-dependent solution of the incompressible Navier–Stokes equations in two and three dimensions, in: Recent Advances in Numerical Methods in Fluids, Pineridge, Swansea, UK, 1980.

[26] FIDAP Theoretical Manual, Fluid Dynamics International, Evanston, IL, 1990.